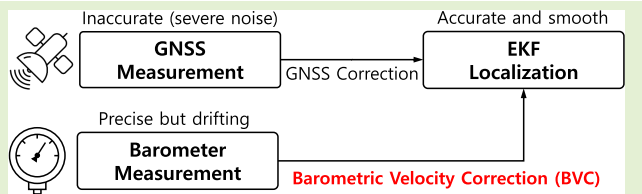


Leveraging GNSS Accuracy With a Barometer

Dongwook Heo, Hyunkil Hwang, Jinwon Choi, and Sunglok Choi^{ID}

Abstract—The global navigation satellite system (GNSS) suffers from vertical accuracy degradation due to satellite geometry and environmental factors. This article proposes a novel barometric velocity correction (BVC) that integrates GNSS and barometric data to improve altitude accuracy. Unlike conventional approaches that treat the barometer as an altitude reference, the proposed BVC uses barometric data as odometric data to estimate vertical velocity, which is integrated into an extended Kalman filter (EKF) framework. Through theoretical analysis, including Kalman gain and uncertainty propagation analysis, we validate the effectiveness and advantages of the BVC. We evaluated the proposed method using comprehensive experiments with synthetic and real-world data. Experiments with synthetic data show that the BVC method significantly improves altitude accuracy, reducing vertical errors by up to 27.6% compared to conventional methods. The proposed BVC method proves particularly effective in handling barometric bias and varying GNSS conditions. Real-world experiments further validate the system's effectiveness, particularly in handling frequent altitude transitions and achieving reliable loop closure where conventional methods exhibit instabilities. This work provides a practical and straightforward sensor integration approach for precise altitude estimation in urban settings with potential applications across various 3-D positioning systems.

Index Terms—Barometer, global navigation satellite system (GNSS), global positioning system (GPS), Kalman filter, localization, positioning system, sensor fusion.



I. INTRODUCTION

GLOBAL navigation satellite system (GNSS) has been widely utilized for outdoor positioning and navigation across various applications, from autonomous vehicles to aircraft. The popularity of GNSS stems from its ability to provide accurate absolute positioning with global coverage. Additionally, the cost of GNSS receivers has become significantly affordable, further driving their applications.

GNSS accuracy can be quantified using the concept of dilution of precision (DOP). Especially, the vertical DOP (VDOP) is typically 1.6–1.8 times larger than the horizontal DOP (HDOP) [1] and can even exceed these values. This disparity highlights the significant influence of VDOP on the overall position DOP (PDOP), indicating that vertical

accuracy is a critical factor in GNSS positioning errors. This limitation arises from the inherent satellite geometry, where GNSS satellites are more widely distributed in the horizontal plane than in the vertical direction, leading to a larger VDOP compared to HDOP. Additionally, errors caused by multipath propagation, ionospheric delays, and weather conditions further exacerbate the difficulty of achieving reliable and accurate GNSS positioning.

Many meaningful works have explored various approaches to improve GNSS accuracy. *Sensor fusion* with additional sensors is typically the first choice. GNSS and the inertial navigation system (INS) were integrated through various approaches such as loosely coupled [2], tightly coupled [3], and factor graph-based methods [4]. Yue et al. [5] and Wang et al. [6] improved 3-D positioning accuracy by integrating the INS and visual odometry with GNSS while detecting and rejecting abnormal measurements. *Prior information*, such as a map, is another valuable resource for enhancing positioning accuracy. Kassas et al. [7] proposed a vehicle location tracking framework that integrates cellular signal pseudoranges and map matching with vector tiles, reducing 3-D positioning errors by 22% in GNSS-enabled environments and by 81% in GNSS-unavailable environments, compared to GNSS/IMU systems. Liu et al. [8] proposed a 3-D LiDAR-aided GNSS-RTK positioning system that combines drift-free point cloud mapping for nonline-of-sight (NLOS) mitigation and virtual satellite generation for improved geometry distribution, achieving submeter positioning accuracy in urban canyons.

Received 31 March 2025; accepted 6 May 2025. Date of publication 16 May 2025; date of current version 2 July 2025. This work was supported by the Ministry of Science and ICT (MSIT)/National Research Foundation of Korea (NRF) Grant for the Bridge Convergence Research and Development Program (AI-based Localization and Path Planning on 3-D Building Surfaces) under Grant 2021M3C1C3096810. The associate editor coordinating the review of this article and approving it for publication was Dr. Sarbjit Paul. (*Corresponding author: Sunglok Choi.*)

Dongwook Heo, Jinwon Choi, and Sunglok Choi are with the Department of Computer Science and Engineering, Seoul National University of Science and Technology (SEOULTECH), Seoul 01811, South Korea (e-mail: hdwook3918@gmail.com; randomkok@seoultech.ac.kr; sunglok@seoultech.ac.kr).

Hyunkil Hwang is with the Department of Mechanical Engineering, University of Delaware, Newark, DE 19716 USA (e-mail: hyunkil76@gmail.com).

This article has supplementary downloadable material available at <https://doi.org/10.1109/JSEN.2025.3568843>, provided by the authors.

Digital Object Identifier 10.1109/JSEN.2025.3568843

However, few studies have focused on improving GNSS accuracy using barometers, despite their high precision, low cost, and compact size. Atmospheric pressure varies with altitude, and the pressure values measured by a barometer can be a valuable source for correcting the vertical position of GNSS. On the other hand, barometric pressure-based altitude estimation faces several challenges. Atmospheric pressure can fluctuate due to weather changes, temperature variations, and local disturbances, which can significantly affect positioning accuracy. These environmental factors are regarded as systematic errors, often modeled as first-order Markov process bias or random constant scale factor errors [9], [10], [11], [12].

In this article, we present a novel approach that enhances altitude estimation by integrating GNSS and barometric measurements through a simple but effective method. Our method utilizes barometric data as vertical velocities, which are then incorporated into a Bayesian filtering framework for robust altitude estimation. Our approach differs from conventional methods by treating the barometer as an *odometric* sensor rather than an absolute or relative altimeter, allowing for more reliable operation in varying atmospheric conditions and subsequent bias errors. In addition, we conducted both quantitative and qualitative evaluations using synthetic and real data, along with additional experiments to validate the assumptions made in barometric velocity calculation.

The remainder of this article is organized as follows. Section II reviews existing approaches to barometer-aided positioning systems. Section III details our proposed method, including the Bayesian localization framework and related mathematical analysis. Sections IV and V present comprehensive experimental results using both synthetic and real-world datasets. Finally, Section VI concludes the article with a summary of our findings and future research directions.

II. RELATED WORKS

Barometers have been utilized to complement GNSS-based positioning systems, particularly to enhance altitude accuracy. In this section, we review previous approaches that integrate barometers for altitude estimation and highlight how our approach differs from these methods.

A. Barometer-Aided Positioning

Barometers have demonstrated their effectiveness across various positioning applications. In aviation, Jan et al. [13] enhanced GNSS-based aircraft landing systems by incorporating barometric measurements. Zhang et al. [14] achieved improved cooperative positioning accuracy for uncrewed aerial vehicles (UAVs) by integrating a barometer with the BeiDou Navigation Satellite System (BDS) and ultrawideband (UWB) systems. For ground vehicles, several methods have utilized barometers to enhance position estimation in GNSS-degraded environments, such as urban areas [12], [15], [16], [17], [18]. Additionally, barometers have proved valuable for indoor altitude estimation and floor detection [19], [20], [21], [22], [23].

Barometer-aided positioning approaches can be categorized into *metric altitude estimation* and *floor-level detection*. Metric altitude estimation determines numerical altitude values in

continuous space, which is essential for applications requiring precise vertical positioning. In contrast, floor-level detection identifies discrete vertical positions, such as building floors or overpass levels, where detecting quantized levels is suitable and sufficient.

Given our focus on precise positioning applications, we focus primarily on metric altitude estimation approaches, which can be divided into two categories based on the use of barometric data: *absolute altitude estimation* and *relative altitude estimation*. Absolute altitude estimation derives absolute altitude from barometric pressure measurements using the mean sea level (MSL) pressure. In contrast, relative altitude estimation calculates relative height changes from a reference point by leveraging the relationship between altitude and pressure in the troposphere.

B. Absolute Altitude Estimation

Converting barometric pressure directly to absolute altitude is the most straightforward approach in barometric altimetry. Several works have explored this direct conversion approach in various applications. Zhang et al. [11] integrated a barometer into a GNSS/INS system to enhance vertical accuracy. They adopted a loosely coupled sensor fusion approach, where barometer bias was corrected using GNSS solutions when satellite geometry was favorable. The corrected barometric altitude was then used to constrain the least-squares estimator in the vertical direction, thereby improving vertical navigation performance. Ge et al. [24] addressed GNSS signal instability in urban environments and INS accumulation errors by incorporating absolute altitude from barometric measurements, achieving smoother trajectory estimates with bounded errors.

However, direct absolute altitude estimation faces several fundamental challenges. First, it heavily depends on an accurate pressure value at the MSL, which can vary significantly with weather conditions. Second, accurate altitude estimation needs to consider the difference between ellipsoidal height and geoid height. The ellipsoidal height refers to the height relative to the Earth's reference ellipsoid, while the geoid height represents the separation between the ellipsoid and the geoid, which approximates the MSL. This difference is critical for precise altitude determination.

1) Standard Sea Level Pressure: The international standard atmosphere (ISA) model [25] has been utilized for direct absolute altitude estimation. The assumption of a fixed sea level pressure works well for high-altitude applications above 4000 m. However, this assumption becomes problematic for low-altitude applications, such as ground vehicles and UAVs in the lower atmosphere. These applications must consider local weather patterns, temperature fluctuations, and pressure anomalies, which significantly affect barometric measurements.

2) Differential Barometer: A pair of barometers have been used as a differential barometer [26], [27] to be free from the fixed sea level pressure assumption. Yun and Park [28] implemented real-time corrections using local weather station pressure data. However, this approach has several limitations. When two barometers are far apart, two distant locations may experience different atmospheric conditions such as pressure and temperature. Furthermore, this approach inevitably

involves complexity and costs associated with synchronization, communication, and maintenance requirements.

C. Relative Altitude Estimation

Relative altitude estimation tracks height changes from a reference point instead of converting barometric pressure to absolute altitude. This approach is quite similar to the concept of differential barometers, but it neither requires the altitude of the reference point nor computes absolute altitude. Consequently, it avoids complications related to MSL pressure assumptions and geoid height corrections adopted in absolute altitude estimation.

Several works have successfully implemented this approach. Park et al. [12] integrated a barometer with GNSS, INS, and odometer systems. Their method involved setting the initial altitude, reference pressure, and temperature under favorable GNSS conditions. Relative altitude was then calculated based on these parameters and added to the initial altitude. This approach improved altitude accuracy by over ten times in environments with obstructed GNSS signals, such as tunnels and underground roads. In this article, we refer to this method as barometric altitude correction with fixed reference (BAC-FR). Chiang et al. [15] also combined a barometer with GNSS, INS, and odometer for highly accurate vehicle localization. Their method used a drift control mechanism based on vehicle driving behavior and reference-based relative altitude estimation. By detecting pitch angle changes, the system controlled altitude changes and maintained altitude accuracy in urban environments with poor GNSS signals during long operations. We refer to this method as BAC with drift control (BAC-DC).

The key advantage of relative altitude estimation is its ability to minimize errors while eliminating the dependence on sea level pressure assumptions and the absolute altitude of the reference point. This relative approach enables seamless integration with GNSS or INS systems without requiring conversions between ellipsoidal and orthometric heights. However, when operating with a single barometer, the approach inevitably accumulates drift error in relative height estimation due to changes in reference pressure over time.

Our Approach: Our proposed method also pursues the relative altitude estimation approach but updates the reference pressure much more frequently. Our method utilizes barometric measurements as *odometric* data by converting them into vertical velocities. Our approach can effectively mitigate the drift effect of atmospheric pressure without requiring precise initial GNSS measurements. Furthermore, these barometric vertical velocities can be seamlessly integrated with GNSS data in the framework of an extended Kalman filter (EKF). Our analysis and experimental results confirm significant improvement in altitude estimation with a single barometer.

III. EKF LOCALIZATION WITH GNSS AND A BAROMETER

A. Problem Formulation

Our objective is to enhance 3-D positioning accuracy by integrating GNSS and barometric data. This integration specifically improves altitude estimation, thereby overcoming the

limitations of GNSS in vertical accuracy. We aim to estimate the 3-D position (x, y, z) without orientation. We do not employ any kinematic constraints (which depend on mobile platforms) to ensure generality and simplicity. As a result, our positioning system outputs the 3-D position (x, y, z) along with the corresponding velocity (v_x, v_y, v_z).

1) GNSS Data: GNSS observations provide 3-D metric position data (x^G, y^G, z^G) in the projected coordinate system (PCS), transformed from the geodetic coordinate system. A GNSS receiver provides geodetic position data (lat, lon, alt) in terms of latitude, longitude, and altitude. Trilateration determines the geodesic position, while altitude estimation requires additional satellites due to uncertainties in satellite geometry [29]. The velocity from GNSS combines pseudorange, Doppler, and carrier-phase techniques [30]. Each measurement technique has inherent limitations. Pseudorange measurements are affected by multipath effects and atmospheric delays. Doppler measurements are sensitive to the signal-to-noise ratio and unreliable at low velocities. Carrier-phase measurements suffer from phase ambiguities and cycle slips. The VDOP is generally worse than the HDOP. In static or low-speed conditions, measurement noise can become larger than the true signal, making it difficult to capture the intended position or velocity data accurately. These limitations can result in signal cut-offs, poor performance, and a lack of vertical velocity estimation, especially at low speeds. Therefore, we utilized barometric data to complement GNSS data.

2) Barometric Data: A barometer provides pressure data P , which measures the atmospheric pressure at a given altitude. Barometric measurements are influenced by various environmental factors such as temperature, atmospheric changes, and humidity. Despite these sensitivities, their high precision and high acquisition frequency make them well-suited for improving degraded GNSS altitude estimation as short-term *odometric* data. In this article, we convert the pressure data into vertical displacements, Δz^B , and vertical velocity, v_z^B . These barometric outputs are integrated into the system to enhance the accuracy of GNSS-based altitude estimation.

B. Barometer Sensor Model

For low-altitude applications, the *barometric altitude formula* [31] can describe the barometric vertical displacement from the reference position to the current position as

$$\Delta z^B(P, P_{\text{ref}}) = \frac{T_{\text{ref}}}{T_{\text{grad}}} \left(1 - \left(\frac{P}{P_{\text{ref}}} \right)^{\frac{R \cdot T_{\text{grad}}}{g}} \right) \quad (1)$$

where P and P_{ref} represent the barometric pressure values at the current and reference positions, respectively. T_{ref} is the absolute temperature at the reference position and T_{grad} is the absolute temperature gradient for altitude, typically given as 0.0065 K/m. The negative sign of T_{grad} is removed for simplicity when deriving this equation. R is the gas constant (287.058 J/K/kg for dry air) and g is the standard gravity (9.80665 m/s²).

Barometric measurements are influenced by various physical factors such as temperature, atmospheric changes, and humidity. The barometric altitude formula cannot fully account

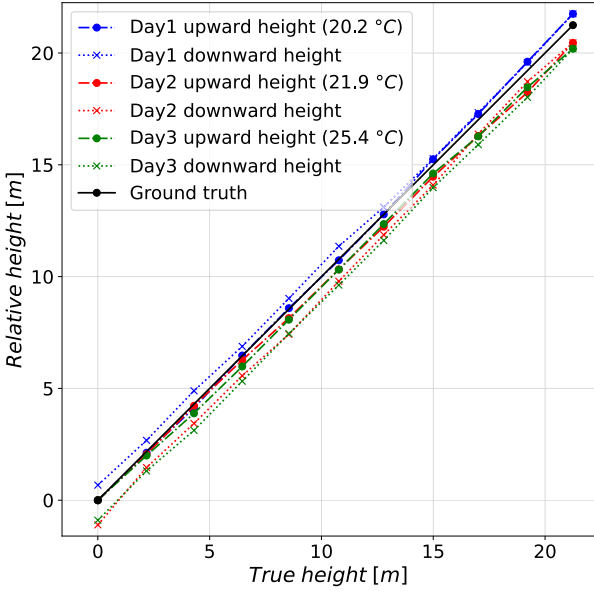


Fig. 1. Relative height estimated from barometric pressure data. Experimental data were collected on various dates and under distinct temperatures (Day 1: 20.2 °C, Day 2: 21.9 °C, and Day 3: 25.4 °C). Three trajectories were acquired in the pattern of ascending (●) to an upper floor and then descending (×) back to the starting floor. Each relative height was calculated from the averaged pressure value over a 10-s interval using (1). The ground-truth data were obtained using a laser altimeter, with the reference floor set to 0 m. Although all trajectories started from the reference floor, a relative height *drift* was observed when returning to the reference floor.

for the complex effects of all these factors, which can lead to errors in altitude estimation. As shown in Fig. 1, our preliminary experiments demonstrated that the formula effectively predicted the slope of relative altitudes. However, they revealed noticeable bias errors, even over relatively short intervals (approximately 10 min). Despite relative height trajectories starting from the reference floor at (0, 0), their final relative height values were shifted from the origin. This observation led us to utilize barometric data as odometric data, rather than absolute or relative altitudes.

C. EKF Localization Framework

Our localization method is based on a discrete-time EKF, a widely recognized approach in Bayesian filtering. The EKF is an extension of the Kalman filter for nonlinear systems. The EKF assumes the probability distribution of the state as Gaussian, which is parameterized as a mean (the state variable \mathbf{x}) and a covariance (the state covariance Σ). In the same manner as other Bayesian filters, it comprises two main steps

$$\text{state prediction: } \bar{\mathbf{x}}_k = f(\mathbf{x}_{k-1}, \mathbf{u}_k) \quad (2)$$

$$\bar{\Sigma}_k = F_{k-1} \Sigma_{k-1} F_{k-1}^\top + Q_k \quad (3)$$

$$\text{state correction: } \mathbf{x}_k = \bar{\mathbf{x}}_k + K_k (\mathbf{z}_k - h(\bar{\mathbf{x}}_k)) \quad (4)$$

$$\Sigma_k = (I - K_k H_k) \bar{\Sigma}_k \quad (5)$$

where k means the k th time step, \mathbf{x} is the state variable, \mathbf{z} is the measurement, and \mathbf{u} is the control input. f and F are the transition function and its Jacobian and h and H are the

observation function and its Jacobian. K is the Kalman gain derived as

$$K_k = \bar{\Sigma}_k H_k^\top (H_k \bar{\Sigma}_k H_k^\top + R_k)^{-1} \quad (6)$$

where Q and R are covariance matrices of transition and observation noises, respectively, both of which are assumed to follow a zero-mean Gaussian distribution. Our EKF localization is primarily based on a constant velocity model and GNSS measurements.

1) EKF Prediction With a Constant Velocity Model: Our state variable describes the 3-D position and velocity, defined as

$$\mathbf{x} = [x \quad y \quad z \quad v_x \quad v_y \quad v_z]^\top. \quad (7)$$

For generality, the state variable does not involve orientation terms and nonholonomic kinematic constraints described in unicycle motion models [32]. Therefore, our transition function is a constant velocity model, defined as

$$\bar{\mathbf{x}}_{k+1} = f(\mathbf{x}_k) = \begin{bmatrix} x_k + v_{xk} \Delta t \\ y_k + v_{yk} \Delta t \\ z_k + v_{zk} \Delta t \\ v_{xk} \\ v_{yk} \\ v_{zk} \end{bmatrix} \quad (8)$$

where Δt is the time interval between the k th and $(k+1)$ th timestamps ($\Delta t = t_{k+1} - t_k$). The transition noise covariance can be assigned as independent noise for each state variable, defined as

$$Q = \text{diag}(\sigma_x^2, \sigma_y^2, \sigma_z^2, \sigma_{v_x}^2, \sigma_{v_y}^2, \sigma_{v_z}^2) \quad (9)$$

where σ_x^2 , σ_y^2 , and σ_z^2 are the variance of position noise, and $\sigma_{v_x}^2$, $\sigma_{v_y}^2$, and $\sigma_{v_z}^2$ are the variance of velocity noise in the corresponding axes. Additionally, the position variance can be derived from the velocity variance [32] using the Jacobian matrix of (8) as follows:

$$Q = \text{diag}(\sigma_{v_x}^2 \Delta t^2, \sigma_{v_y}^2 \Delta t^2, \sigma_{v_z}^2 \Delta t^2, \sigma_{v_x}^2, \sigma_{v_y}^2, \sigma_{v_z}^2). \quad (10)$$

2) EKF Correction With Adaptive GNSS Noise Covariance: The GNSS measurement is given as

$$\mathbf{z}^G = [x^G \quad y^G \quad z^G]^\top \quad (11)$$

and its observation function is defined as

$$\mathbf{z}^G = h^G(\mathbf{x}) = H^G \mathbf{x}, \quad \text{where } H^G = [I_{3 \times 3} \ 0_{3 \times 3}]. \quad (12)$$

The GNSS receiver provides position data in different modes: RTK-Fixed, RTK-Float, DGNSS, and SPS. Each positioning mode exhibits distinct accuracy characteristics. The RTK-Fixed mode typically provides centimeter-level accuracy, but the other modes result in significantly degraded accuracy and reliability, especially in the vertical component. Our experimental observations indicate that altitude measurements can become quite unreliable even in the RTK-Float mode. Therefore, it is necessary to adjust the GNSS noise covariance dynamically according to the GNSS positioning mode. The observation noise covariance can be defined as

$$R_k^G = \text{diag}((\sigma_{x,k}^G)^2, (\sigma_{y,k}^G)^2, (\sigma_{z,k}^G)^2) \quad (13)$$

where $(\sigma_{x,k}^G)^2$, $(\sigma_{y,k}^G)^2$, and $(\sigma_{z,k}^G)^2$ are the GNSS variance for each direction at the k th time step. This indicates that the variances are time-varying rather than constant, adapting to changes in the GNSS positioning mode. In our implementation, we acquired GNSS data using `nmea_nasat_driver` in ROS 2, which provided GNSS data with their heuristic covariance assignment based on the positioning mode and HDOP.

D. Conventional BAC

1) *BAC With a Fixed Reference*: The BAC-FR [12] utilizes the initially assigned reference altitude and pressure values to enhance inaccurate altitude values of GNSS data. At the initialization stage, BAC-FR sets its reference altitude z_{ref} and pressure P_{ref} as the average of one minute of stationary GNSS and barometer data. BAC-FR calculates the relative altitude Δz_B using (1) and adds it to the reference altitude to get the current altitude observation, which can be expressed as

$$\mathbf{z}_k^{\text{BAC}} = [z_{\text{ref}} + \Delta z^B(P_k, P_{\text{ref}})]. \quad (14)$$

The current altitude observation is applied to the EKF correction step, as shown in (4). Its observation function and noise covariance can be defined as

$$\mathbf{z}_k^{\text{BAC}} = h^{\text{BAC}}(\mathbf{x}_k) = H^{\text{BAC}} \mathbf{x}_k \quad (15)$$

$$H^{\text{BAC}} = [0 \ 0 \ 1 \ 0 \ 0 \ 0] \quad (16)$$

$$R^{\text{BAC}} = [(\sigma_z^B)^2]. \quad (17)$$

BAC-FR can provide reasonable altitude observations initially.

However, BAC-FR does not fundamentally solve the altitude drift problem. As shown in Fig. 1, the altitude observations exhibit drift errors over time, eventually leading to significant bias in altitude estimation.

2) *BAC With Drift Control*: BAC-DC [15] improves altitude estimation by mitigating altitude drift in GNSS-degraded environments. To reduce the altitude drift, BAC-DC employs a motion constraint for altitude updates, requiring apparent upward or downward changes in the pitch angle. BAC-DC also calculates relative altitude using (1), but it separates its calculation into two cases (*height-resting* and *height-changing*) as follows:

$$\Delta z_k^{\text{DC}}(P_k, P_{\text{ref}}) = \begin{cases} E(\Delta z_{k-n:k-1}^{\text{DC}}), & \text{if } |\theta_k| \leq \tau_\theta \\ \Delta z^B(P_k, P_{\text{ref}}), & \text{if } |\theta_k| > \tau_\theta \end{cases} \quad (18)$$

where θ_k is the pitch angle at the k th time step and $\Delta z_{k-n:k-1}^{\text{DC}}$ is a series of values from $\Delta z_{k-n}^{\text{DC}}$ to $\Delta z_{k-1}^{\text{DC}}$. The function E calculates the average of the given values, and τ_θ is the threshold to distinguish between height-resting and height-changing cases. In the height-changing case, relative altitude is computed in the same way as BAC-FR. In the height-resting case, barometric data are not used directly. Instead, relative altitude is derived from the exponential moving average of the last n data in the queue. Similar to BAC-FR, the observation variable and function for BAC-DC are the same as (14)–(17) except for replacing $\Delta z^B(P_k, P_{\text{ref}})$ with $\Delta z_k^{\text{DC}}(P_k, P_{\text{ref}})$.

Although BAC-DC reduces altitude drift by identifying *height-resting*, it has several limitations. First, it does not

fully resolve the altitude drift problem. It does not update the reference pressure P_{ref} online, which is initialized only once and remains unchanged thereafter. Moreover, it does not address altitude drift during the *height-changing* case. Our experiments included long periods of height-changing, and BAC-DC produced the same results as BAC-FR during these periods. Second, BAC-DC requires pitch angle information, necessitating additional sensors such as IMUs or tilt sensors. In our real experiments, we used an attitude and heading reference system (AHRS) to retrieve the pitch angle data.

E. Proposed BVC

We propose the barometric *velocity* correction as an alternative to the conventional barometric *altitude* correction. Barometric velocity is derived from the current and previous pressure values, which means that our method updates the reference pressure in every time step, as given in (1). Additionally, our method does not require a reference altitude. These two features enable our approach to effectively overcome altitude drift commonly observed in the previous BAC methods.

1) *Motivation*: As shown in Fig. 1, barometric vertical displacement can be modeled with bias and white noise as follows:

$$\Delta z^B(P_k, P_{\text{ref}}) = \Delta z^{\text{GT}} + b_z^B(t_k - t_{\text{ref}}) + \epsilon_z^B \quad (19)$$

where b_z^B represents a bias error factor and ϵ_z^B are unbiased Gaussian random variables. It is evident that the vertical displacement accumulates bias over time, leading to increasing errors as t_k progresses. To address this issue, we instead consider barometric vertical velocity, which can be expressed as

$$v_z^B(P_k, P_{k-1}) = \frac{\Delta z^B(P_k, P_{k-1})}{\Delta t} = v_z^{\text{GT}} + b_z^B + \frac{\epsilon_z^B}{\Delta t}. \quad (20)$$

Unlike the displacement, the velocity error does not accumulate over time, making it a more reliable representation of barometric data. Although a bias error b_z^B exists, it remains constant and is significantly small as our empirical observation. This motivates our choice of vertical velocity over vertical displacement for barometric correction.

2) *Barometric Velocity Correction*: Our EKF state correction is performed with barometric velocity observation instead of barometric altitude observation. We refer to our method as barometric velocity correction (BVC). Barometric vertical velocity, as defined in (20), is calculated from two consecutive pressure values, P_k and P_{k-1} , and their time interval, Δt . In our implementation, the reference pressure is dynamically assigned as the previous pressure value, rather than a fixed initial value. The barometric velocity observation is defined as

$$\mathbf{z}_k^{\text{BVC}} = [v_z^B(P_k, P_{k-1})]. \quad (21)$$

Significantly, the barometric velocity observation does not involve the reference altitude in contrast to (14). Its corresponding observation function and noise covariance are expressed as

$$\mathbf{z}_k^{\text{BVC}} = h^{\text{BVC}}(\mathbf{x}_k) = H^{\text{BVC}} \mathbf{x}_k \quad (22)$$

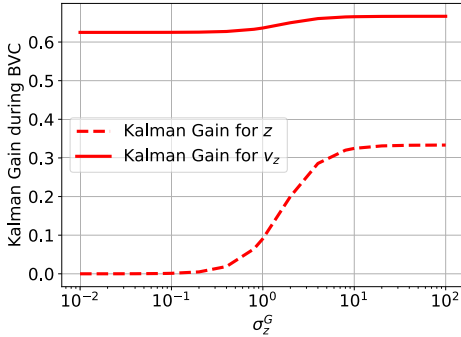


Fig. 2. Kalman gain during the BVC. The Kalman gain was derived after a single step of state prediction and GNSS correction under the default noise setting, where all values were set to one for simplicity. Its weight coefficients for z and v_z [as expressed in (26)] were visualized with varying GNSS noise σ_z^G and a fixed barometric velocity noise of $\sigma_{v_z}^B = 1$.

$$H^{BVC} = \begin{bmatrix} 0 & 0 & 0 & 0 & 0 & 1 \end{bmatrix} \quad (23)$$

$$R_k^{BVC} = \left[(\sigma_{v_z,k}^B)^2 \right]. \quad (24)$$

When the noise variance of pressure values is denoted as $(\sigma_p^B)^2$, its corresponding noise variance of the vertical velocity can be derived as

$$(\sigma_{v_z,k}^B)^2 = \frac{\alpha_k^2}{\Delta t^2} (\sigma_p^B)^2, \quad \text{where } \alpha_k = \frac{\partial \Delta z^B(P, P_{k-1})}{\partial P} \Bigg|_{P=P_k}. \quad (25)$$

In the standard atmosphere configuration ($P = 1013.25$ hPa), α_k is derived to be approximately -0.083 . Additionally, we observed that α_k remains nearly constant for consecutive pressure configurations. Specifically, the difference of α_k is limited to just 0.00013 when two pressure values differ by up to ± 100 Pa.

The barometer correction with v_z^B effectively acts as a vertical odometer, offering continuous estimates of vertical velocity, even in GNSS-degraded environments. Since our proposed correction updated the reference pressure value and does not use the reference altitude, it can effectively deal with altitude drift. This capability is particularly valuable in scenarios where GNSS signals are inaccurate and unreliable due to multipath effects or signal blockage.

3) Kalman Gain Analysis: The weighting factor for barometric velocity can be dynamically adjusted according to the magnitude of GNSS noise. It enables adaptive fusion that enhances the accuracy of vertical position and velocity. The Kalman gain plays a crucial role in determining the weight distribution between predicted states and measurement corrections, directly influencing estimation performance. A higher Kalman gain value indicates greater confidence in the measurement compared to the prediction. We symbolically derived the Kalman gain K [see (6)] during the proposed BVC and visualized its weighting factors for z and v_z in Fig. 2. For simplicity, we set all other configuration variables to one. For instance, the state covariance matrix was initialized as an identity matrix, and all transition noise parameters were configured as $Q = \text{diag}(1, 1, 1, 1, 1, 1)$. After state prediction

and correction using GNSS measurements, the Kalman gain for the BVC was derived as $K = \text{diag}(0, 0, w_z, 0, 0, w_{v_z})$, where

$$w_z = \frac{1}{\beta} (\sigma_z^G)^2 \text{ and } w_{v_z} = \frac{1}{\beta} \left\{ 2(\sigma_z^G)^2 + 5 \right\}, \quad \text{where} \\ \beta = (\sigma_{v_z}^B)^2 (\sigma_z^G)^2 + 3(\sigma_{v_z}^B)^2 + 2(\sigma_z^G)^2 + 5. \quad (26)$$

Fig. 2 illustrates the Kalman gain with $\sigma_{v_z}^B = 1$. It clearly shows that the weighting of barometric velocity increases as GNSS noise worsens (i.e., when σ_z^G is larger). For instance, barometric velocity plays a more significant role when GNSS operates in the DGNSS or SPS mode, whereas its influence decreases in the RTK-Fix mode due to higher GNSS accuracy. This analysis shows how the BVC offers adaptability when integrating with GNSS-degraded conditions.

4) Uncertainty Propagation Analysis: The BVC enables a less uncertain estimate of vertical position and velocity compared to GNSS-only correction and BAC. This improvement leads to more accurate localization in vertical position and velocity. In the EKF framework, the uncertainty of state variables is quantified by the state covariance Σ . Previous works have analyzed state covariances analytically [33] and experimentally [32] to assess state uncertainty in the EKF framework. Choi and Kim [33] examined off-centered GPS observation, while Na et al. [32] explored various motion models. In this article, we initialized the state covariance as an identity matrix and symbolically performed a single iteration of state prediction, GNSS correction, and BVC. The state covariance was propagated before applying the state correction. For simplicity, all parameters were set to one except for σ_z^G and $\sigma_{v_z}^B$. Two key diagonal elements of the 6×6 covariance matrix are derived as

$$\Sigma_{(3,3)} = \frac{1}{\beta} \left\{ 8(\sigma_{v_z}^B)^2 (\sigma_z^G)^2 + 8(\sigma_{v_z}^B)^2 + 7(\sigma_z^G)^2 + 5 \right\} \quad (27)$$

$$\Sigma_{(6,6)} = \frac{1}{\beta} \left\{ 3(\sigma_{v_z}^B)^2 (\sigma_z^G)^2 + 8(\sigma_{v_z}^B)^2 + 2(\sigma_z^G)^2 + 5 \right\} \quad (28)$$

where $\Sigma_{(r,c)}$ denotes the element at the r th row and c th column of the covariance matrix. A similar derivation with the same configuration was also conducted for BAC. Fig. 3 presents the two diagonal elements for z and v_z estimates by three methods: GNSS-only correction, BAC, and BVC. As expected, GNSS-only correction yields uncertainty independent of barometric noises. Both BAC and BVC provide less uncertain estimates for z and v_z when barometric noises are lower than 10. In particular, the BVC produces significantly less uncertain estimates compared to BAC.

IV. EXPERIMENTS WITH SYNTHETIC DATA

We conducted comprehensive experiments using synthetic data to thoroughly evaluate the performance and characteristics of our proposed method. The synthetic data allow us to validate the experimental performance of the proposed localization and assess accuracy under controlled conditions with established ground truth. The synthetic data were designed to simulate various challenging scenarios, including different GNSS modes and barometric bias. These synthetic experiments enable quantitative accuracy evaluation and systematic comparison with existing methods.

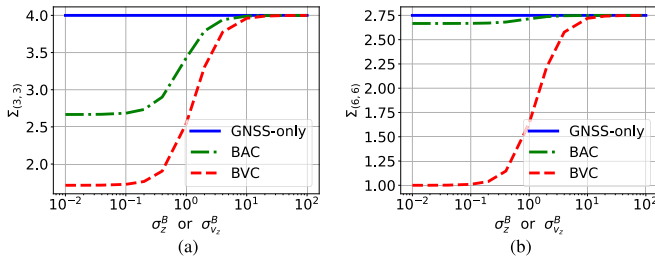


Fig. 3. Uncertainty propagation after the BAC and BVC. The state covariance was derived after EKF prediction and correction steps under the default noise setting. The uncertainties for z and v_z were illustrated with varying barometric noises (σ_z^B for the BAC and $\sigma_{v_z}^B$ for the BVC) and fixed GNSS noise of $\sigma_z^G = 1$. (a) Uncertainty in z . (b) Uncertainty in v_z .

A. Configuration

1) *Data Generation*: GNSS and barometric pressure measurements were generated based on a predefined virtual trajectory. Fig. 4 illustrates the synthetic trajectory.

This trajectory was designed to emphasize altitude variations to thoroughly evaluate 3-D positioning accuracy. The synthetic trajectory spanned about 220 s, with the data points sampled at 10 Hz. The horizontal trajectory formed a square-shaped loop consisting of four linear segments interconnected by curved transitions at each corner. The vertical profile comprised alternating ascending and descending segments.

We designed three experimental scenarios with progressively increasing levels of complexity. The first case (referred to as *Case 1*) incorporates unbiased Gaussian noise in both GNSS and barometric measurements, as illustrated by Fig. 4(a)–(c). In the second case (referred to as *Case 2*), barometric bias is introduced alongside unbiased Gaussian noise, as shown in Fig. 4(f). In the third case (referred to as *Case 3*), time-varying GNSS modes are applied to GNSS measurements, as demonstrated in Fig. 4(d) and (e). This data generation approach effectively simulates the characteristic behaviors of both GNSS and barometer data in real-world environments.

Synthetic GNSS measurements were generated with unbiased Gaussian noise as follows:

$$x_k^G = x_k^{GT} + \mathcal{N}(0, (\sigma_{x,k}^G)^2) \quad (29)$$

$$y_k^G = y_k^{GT} + \mathcal{N}(0, (\sigma_{y,k}^G)^2) \quad (30)$$

$$z_k^G = z_k^{GT} + \mathcal{N}(0, (\sigma_{z,k}^G)^2) \quad (31)$$

where $(x_k^{GT}, y_k^{GT}, z_k^{GT})$ represents the ground-truth position along the synthetic trajectory at the k th time step, and $\mathcal{N}(0, \sigma^2)$ denotes a Gaussian random variable with zero mean and specific variance σ^2 . The GNSS noise variances were time-varying to simulate different GNSS modes, as shown in Fig. 4(d) and (e). We considered four distinct GPS modes: RTK-Fix, RTK-Float, DGNSS, and SPS. Their magnitudes of GNSS noise were based on the specification of the GNSS system employed in our real experiments. The horizontal noise magnitudes σ_x^G and σ_y^G were set as (0.001, 0.0025, 0.017, 1) in the order of RTK-Fix, RTK-Float, DGNSS, and SPS. Similarly, the vertical noise magnitude σ_z^G was defined as

(0.01, 0.04, 0.27, 3) in the same order. In Cases 1 and 2, their GNSS mode remained DGNSS, whose noise magnitude was configured as $(\sigma_x^G, \sigma_y^G, \sigma_z^G) = (0.017, 0.017, 0.27)$. In Case 3, its GNSS mode was sequentially switched from RTK-Fix to RTK-Float, DGNSS, and finally SPS. The synthetic GNSS measurements were generated at 10 Hz, corresponding to the GNSS receiver used in our real experiments.

Synthetic barometric pressures were simulated to reflect altitude changes along the synthetic trajectory. The pressure measurements were produced with unbiased Gaussian noise and bias error that accumulated over time as follows:

$$P_k = P_k^{GT} + \mathcal{N}(0, (\sigma_P^B)^2) + b_P^B(t_k - t_0) \quad (32)$$

where P_k^{GT} is the ground-truth pressure at the k th time step. The unbiased noise magnitude σ_P^B was assigned as 0.01 hPa, and the biased noise factor b_P^B was set to 0.032 Pa/s. Both values were determined based on the specification and empirical data of the barometer used in our real experiments. The synthetic pressure measurements were also generated at 10 Hz.

2) *Parameter Configuration*: The accuracy of an EKF-based localization method is dependent on its parameter configuration. To determine the optimal parameters, we employed a *grid search* approach. Since we already knew about the statistical characteristics of synthetic GNSS and barometric data, we focused on the transition noise covariance Q . In particular, σ_z and σ_{v_z} are crucial factors influencing altitude accuracy when integrating barometric data. Our grid search systematically explored a wide range of parameter values spanning multiple orders of magnitude to identify the optimal parameter combination that minimizes positioning errors. Fig. 5 illustrates an example of our grid search in the third synthetic data scenario (Case 3). Fig. 6 provides a comprehensive summary of the grid search results across four localization methods and three synthetic scenarios.

3) *Evaluation Metrics*: The accuracy of each localization method is evaluated using positional and altitude errors. Since ground-truth values are available in the synthetic data, these errors are defined as follows:

$$e_p,k = \| \mathbf{p}_k - \mathbf{p}_k^{GT} \|_2 \quad (33)$$

$$e_z,k = |z_k - z_k^{GT}| \quad (34)$$

where $\mathbf{p} = [x, y, z]^\top$ and $\mathbf{p}^{GT} = [x^{GT}, y^{GT}, z^{GT}]^\top$ represent the estimated and ground-truth positions, respectively. e_p represents the 3-D positional error, while e_z denotes the altitude error specified only to the Z-direction. Each trajectory consists of multiple positions, so we computed the median as follows:

$$e_p = \text{median}(e_{p,1}, \dots, e_{p,N}) \quad (35)$$

$$e_z = \text{median}(e_{z,1}, \dots, e_{z,N}) \quad (36)$$

where N is the length of the given trajectory. The median metric provides a robust summary of the overall error, making it less sensitive to outliers—an essential consideration when evaluating localization performance in challenging GNSS-degraded scenarios. As shown in Fig. 7, we also present the entire error distribution to analyze accuracy across every time step along each trajectory.

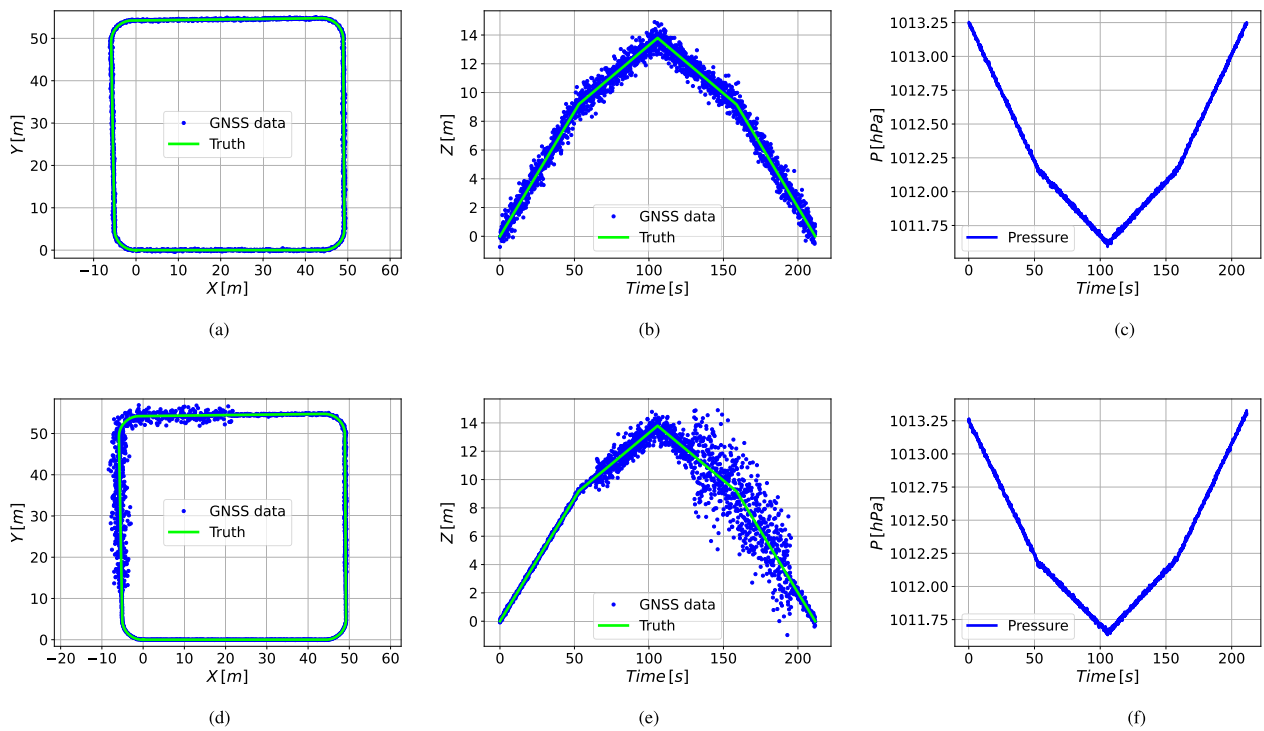


Fig. 4. Trajectories and sensor data of synthetic data. The trajectory begins at the origin (0, 0, 0) and moves along the X -axis while rotating counterclockwise and ascending (later descending). (a) and (b) Fixed noise variances in GNSS data, while (c) unbiased barometer data. (d) and (e) Varying noise variance in GNSS data and (f) biased barometer data.

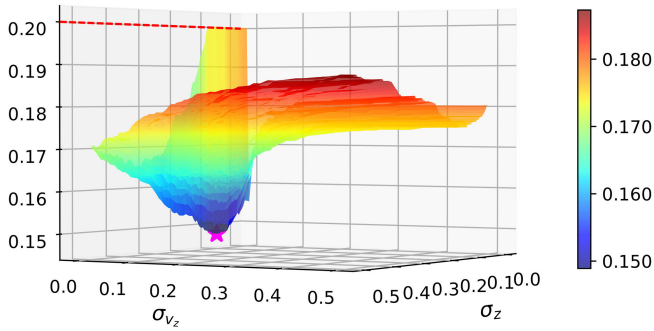


Fig. 5. Example of grid search to find the optimal parameters. Various combinations of parameters (σ_z and σ_{v_z}) were applied to each localization method to determine their optimal values. The accuracy of each combination was evaluated using the median positional error e_p across all time steps. As a result, the grid search identified $\sigma_z = 0.1$ and $\sigma_{v_z} = 0.01$ as the optimal parameters (denoted as *) for the third synthetic data case.

TABLE I
MEDIAN POSITION AND ALTITUDE ERRORS (e_p , e_z) FOR EACH METHOD AND EXPERIMENTAL CASE (UNIT: METER)

Methods		Case 1		Case 2		Case 3		
		e_p	e_z	e_p	e_z	e_p	e_z	
GNSS-only [34]		0.122	0.082	0.122	0.082	0.111	0.070	
GNSS + Barometer		BAC-FR [12]	0.104	0.060	0.120	0.082	0.086	0.055
		BAC-DC [15]	0.104	0.060	0.120	0.082	0.086	0.055
		BVC (ours)	0.101	0.052	0.100	0.050	0.089	0.039

B. Results and Discussion

Table I shows the overview of the experimental results in the synthetic data. Our proposed BVC achieved nearly 5.9% lower position errors and 27.6% lower altitude errors compared to

two conventional BAC methods. Positional errors also account for horizontal errors, which were the same across all methods (0.068, 0.068, and 0.055 m, respectively, in each case), so the difference in positional errors is less significant than altitude errors. Since our synthetic trajectory continuously changed in altitude, BAC-DC always operated in the *height-changing* mode, resulting in the same performance as BAC-FR.

Fig. 7 demonstrates the distribution of all altitude errors in the given synthetic data. These comprehensive results also confirm the superiority of the proposed BVC over the two BAC methods. Each median altitude error in Table I corresponds to the line $y = 0.5$.

1) *Three Experimental Cases*: In all three cases, the BVC demonstrated the best accuracy compared to the other three methods. The altitude error reduction achieved by the BVC was nearly 13.7%, 38.8%, and 30.4% better than the two BAC methods. As mentioned earlier, the three cases include unbiased Gaussian noise (for Case 1), additional biased barometric noise (for Case 2), and additional varying GNSS modes (for Case 3). The proposed BVC outperformed the BAC methods in all three scenarios.

In particular, the improvement was especially notable in Cases 2 and 3, which include bias in barometric data, compared to Case 1. This observation indicates that the BVC was more effective at handling biased barometric noise compared to the BAC methods. In Case 2, both BAC methods exhibited worse accuracy than the GNSS-only method, revealing that the BAC methods have fundamental limitations in handling drift errors in barometric data.

As shown in Fig. 8, barometric data were effective, particularly under worse GNSS noise conditions. More severe

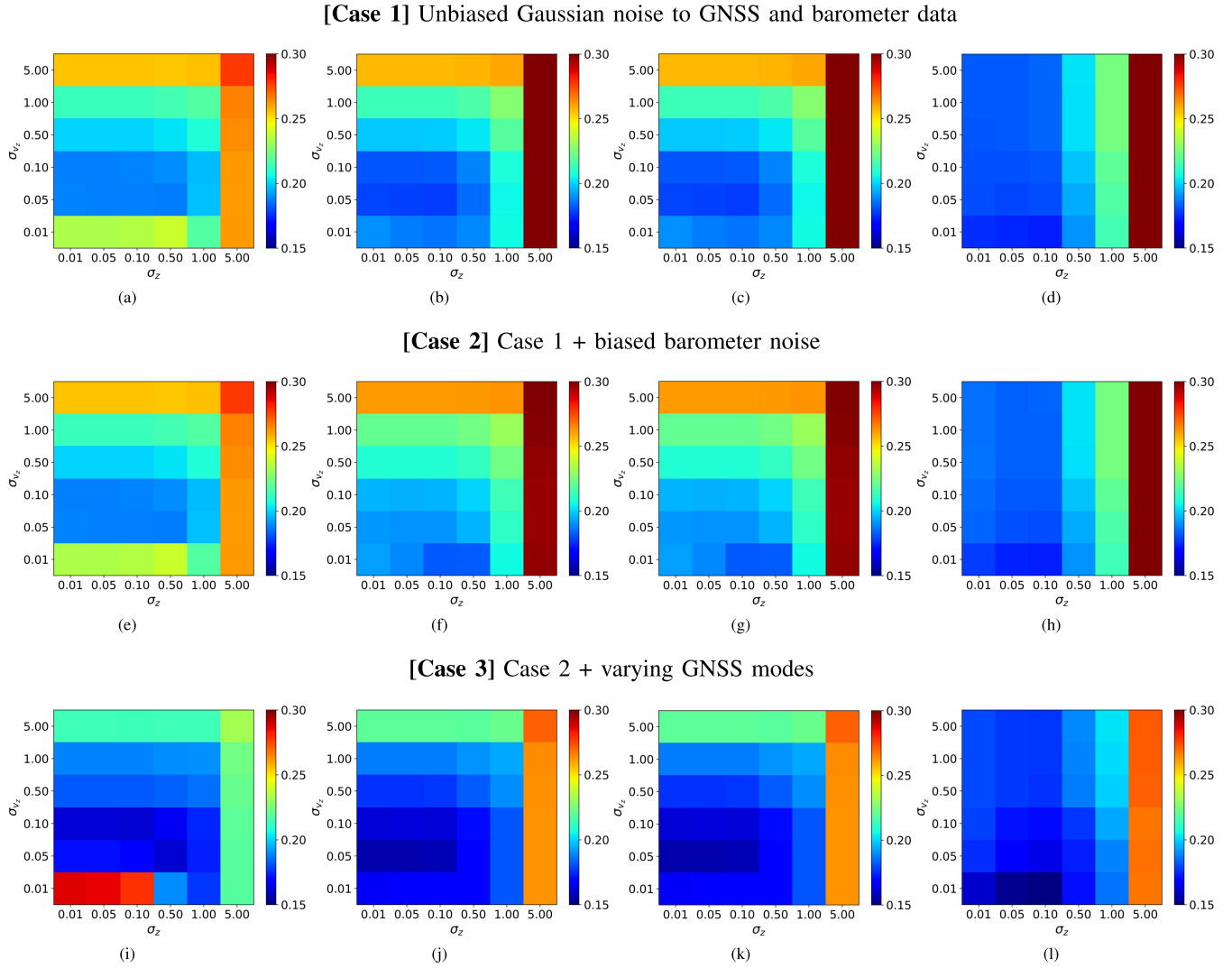


Fig. 6. Heat maps of median positional errors e_p for different vertical transition noise settings. Each heat map represents the median positional error e_p for a specific method and experimental scenario. Lower values (blue) indicate higher accuracy, while higher values (red) mean lower accuracy. (a), (e), and (i) GNSS-only [34]. (b), (f), and (j) BAC-FR [12]. (c), (g), and (k) BAC-DC [15]. (d), (h), and (l) BVC (ours).

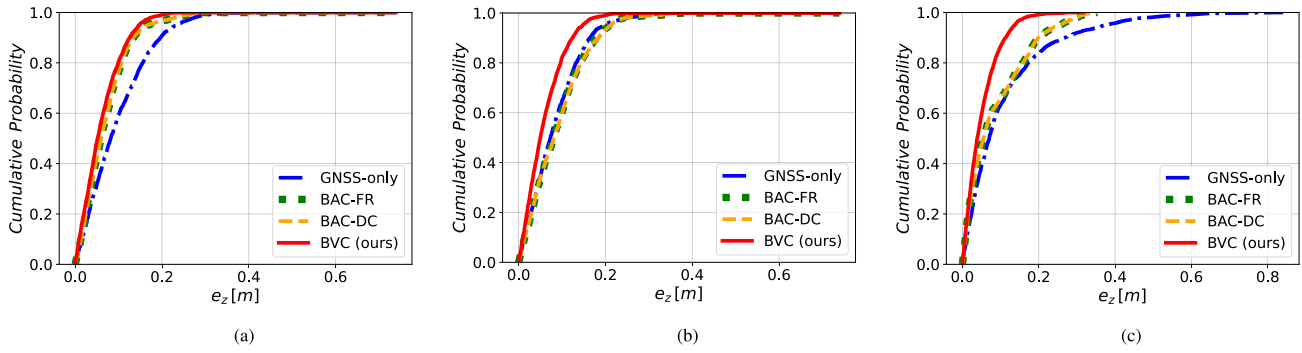


Fig. 7. Cumulative probability distribution of all altitude error values $e_{z,k}$ in the given synthetic trajectory. Each cumulative probability distribution is derived from $y = \Pr(e_{z,k} \leq x)$ for a specific method and case. The steepness of a curve serves as a key performance indicator of higher accuracy. (a) Case 1. (b) Case 2. (c) Case 3.

GNSS noise was applied to our synthetic data after 120 s. GNSS-only localization exhibited a more fluctuating altitude trajectory, while the BAC and BVC methods maintained much cleaner trajectories. In addition, the biased altitude estimates of the two BAC methods can be observed in Fig. 8(b) and (c).

On the other hand, all methods (including the GNSS-only, BAC-FR, BAC-DC, and BVC) in Table I had better positional and altitude accuracies in Case 3 than their corresponding values in Cases 1 and 2. This result stemmed from our GNSS noise setting in Case 3, which included not only higher

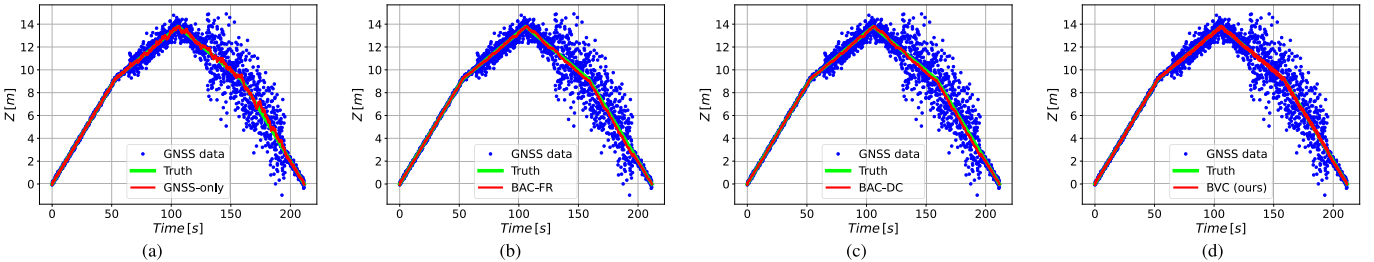


Fig. 8. Altitude estimates of each method in Case 3. The GNSS modes were switched among RTK-Fix, RTK-Float, DGNSS, and SPS. After 120 s, the most severe GNSS noise was applied to simulate the SPS mode. (a) GNSS-only [34]. (b) BAC-FR [12]. (c) BAC-DC [15]. (d) BVC (ours).

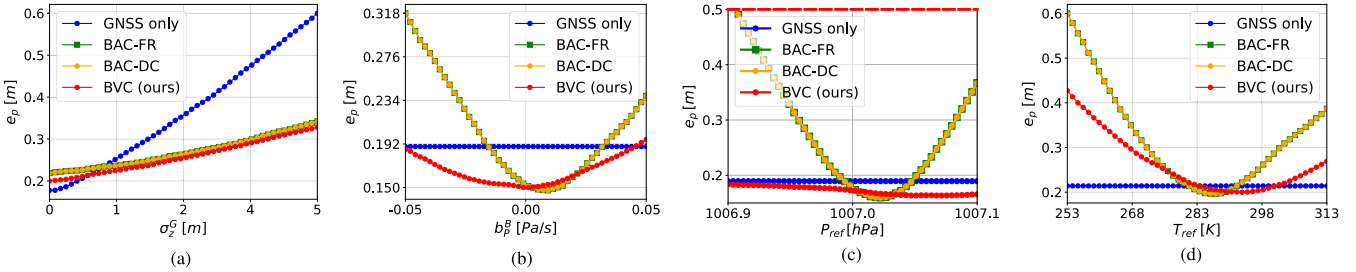


Fig. 9. Median position error e_p changes according to different control variables. By default, we configured $\sigma_z^G = 1$ m, $\sigma_p^B = 0.01$ hPa, $b_p^B = 0.032$ Pa/s, $P_{\text{ref}} = 1007$ hPa, and $T_{\text{ref}} = 292.35$ K. The range of each control variable is shown on the X-axis of the corresponding plot. In (b) and (c), the median position error of GNSS-only localization remains constant because it is independent of barometers. (a) e_p to varying σ_z^G . (b) e_p to varying b_p^B . (c) e_p to varying P_{ref} . (d) e_p to varying T_{ref} .

GNSS noise but also lower GNSS noise. Our GNSS noise configurations are visualized in Fig. 4(b) and (e).

2) Sensitivity to Transition Noise Setting: Our proposed BVC was less sensitive to the transition noise setting. The transition noise covariance Q is one of the crucial parameters of performance in EKF-based localization. As shown in Fig. 6, the proposed BVC maintained lower positional errors with a wider range of parameter space (σ_z , σ_{v_z}) than the other three methods. The error values of the other methods were quite sensitive to the variation of the transition noise setting. This sensitivity analysis suggests that the proposed BVC provides a more reliable and structurally stable parametrization of barometric data. This observation was consistent across all three experimental cases.

3) Magnitude of GNSS Noise: Both the BVC and BAC were more effective when the magnitude of GNSS noise became more severe. Fig. 9(a) presents the median positional error e_p for the varying magnitude of GNSS noise in the Z-axis, σ_z^G . Under the default barometric noise configuration ($\sigma_p^B = 0.01$ hPa and $b_p^B = 0.032$ Pa/s), BVC, BAC-DC, and BAC-FR achieved lower positional error when $\sigma_z^G > 0.5$ m. As expected, the BVC always demonstrated higher accuracy compared to the two BAC methods. When GNSS noise was quite small, barometric data were no longer beneficial because localization could already achieve sufficiently high accuracy without barometric data.

4) Magnitude of Biased Barometric Noise: The BVC was more resistant to biased barometric noise. Fig. 9(b) presents the median positional error e_p for the varying magnitude of biased barometric noise, b_p^B . While the BAC methods became significantly inaccurate even for small values of b_p^B , the BVC maintained better accuracy than GNSS-only localization when

$|b_p^B| < 0.05$ Pa/s. This result confirms that the BVC is less affected by biased barometric noise.

5) Uncertainty of Reference Pressure: The BVC was more stable to the uncertainty of the reference pressure in the barometric altitude formula [see (1)]. Fig. 9(c) illustrates the median positional error e_p for varying values of the reference pressure, P_{ref} . Surprisingly, even minor pressure deviations of 8 Pa resulted in significant positional errors, showing an increase of 65%–156% for BAC methods. However, the proposed BVC maintained better performance than conventional methods by dynamically updating the reference pressure. Notably, the method demonstrated resilience to initial pressure differences of up to 50 Pa while maintaining stable performance.

6) Uncertainty of Reference Temperature: The BVC was also robust to the uncertainty of the reference temperature in the barometric altitude formula [see (1)]. Fig. 9(d) demonstrates the median positional error e_p for varying values of the reference temperature, T_{ref} . As expected, a larger temperature deviation led to an increase in positional errors. However, the proposed BVC was relatively robust within a temperature range of ± 10 K from the true value.

V. EXPERIMENTS WITH REAL DATA

We performed real-world experiments to validate the effectiveness of our proposed method. While synthetic experiments provided controlled conditions for quantitative validation, real-world testing introduces additional challenges such as unexpected GNSS signal degradation and atmospheric pressure drift. The real-world experiments also allow us to observe the system's ability to handle unexpected sensor behavior and environmental disturbances commonly encountered in practical applications.



Fig. 10. Testbed 1. A road view image [35] of Testbed 1 shows the complex urban environment with multistory buildings and trees near the experimental site. Our test area is highlighted in cyan color.

A. Configuration

1) Sensor Setup: We integrated the necessary sensors into a custom-designed sensor box and ROS 2 middleware to ensure synchronized data collection. The sensor suite consisted of a u-blox ZED-F9R GNSS receiver, a Stereolabs ZED 2i (especially its internal barometer) for atmospheric pressure acquisition, and a WithRobot myAHRS+ for inertia–magnetic attitude estimation (only for BAC-DC). All sensors were rigidly mounted with careful calibration of their relative positions and orientations to maintain consistent spatial relationships throughout the experiments. All sensor measurements were collected with ROS 2 Humble, ensuring synchronized data collection and subsequent data processing.

2) Testbeds: The experimental validation was conducted across two distinct locations, each presenting unique environmental challenges.

The first testbed (referred to as *Testbed 1*) was an urban environment near Hanyang Women's University ($37^{\circ}56'N$, $127^{\circ}04'E$), Seoul, Republic of Korea, as shown in Fig. 10. Testbed 1 featured constant elevation variations with an inclination angle of approximately 7° , along with urban canyon effects caused by surrounding buildings. Its environmental complexity was further increased by vegetation affecting GNSS signal propagation and urban infrastructure causing multipath effects.

The second testbed (referred to as *Testbed 2*) was an open field environment in Seoul National University of Science and Technology (SEOULTECH), ($37^{\circ}63'N$, $127^{\circ}08'E$), Seoul, Republic of Korea, as shown in Fig. 11. Testbed 2 featured more diverse slope variations and complex elevation changes compared to Testbed 1. The longer experiment duration in this open environment enabled us to focus on investigating barometer bias effects while maintaining reliable GNSS signals.

3) Trajectories and Sensor Data: The trajectory in Testbed 1 consisted of a straight go-and-return with a loop for closure. Fig. 12(a) and (b) shows the XY plane and vertical trajectories in Testbed 1, demonstrating GNSS signal characteristics primarily in RTK-Fix and RTK-Float positioning modes. The measured trajectory follows a linear reciprocating motion



Fig. 11. Testbed 2. A drone view image [36] of Testbed 2 presents an open field with no buildings or trees in its surroundings. Our test area is marked in orange color.

along a sloped path, covering a distance of approximately 17 m with an elevation change of 3 m. The path was traversed once in both forward and backward directions, returning to the initial starting point. During the initial 5 s of measurement, the GNSS-derived altitude data exhibited an abnormal upward trend, while the actual trajectory moved downward. Additionally, an abrupt change in altitude measurement occurred at approximately 13 s, despite continuous GNSS signal reception. Fig. 12(c) shows that barometric measurements, although affected by inherent bias, consistently reflected the actual altitude changes.

The trajectory in Testbed 2 included a rectangular closed loop with various slope changes. Fig. 12(d) and (e) illustrates the trajectory in both the horizontal plane and vertical direction, showing a rectangular path with consistently high-quality GNSS signal reception. In contrast to Testbed 1, this trajectory exhibited more diverse altitude variations without any abnormal signals throughout the measurement period. The data collection spanned approximately 190 s, covering a vertical displacement of about 9 m and a horizontal distance of approximately 100 m. Similar to Testbed 1, the barometric measurements contained more apparent bias, as shown in Fig. 12(f).

4) Evaluation Criteria: In the absence of ground-truth trajectory data, we utilized geometric constraints of the trajectories for accuracy evaluation. The experimental trajectories were designed to include either linear paths with constant gradients or closed-loop patterns with repetitive elements. These geometric constraints enabled the assessment of the accuracy and reliability of localization algorithms.

For qualitative evaluation, we considered the following two aspects. First, we analyzed trajectory consistency, focusing on loop closure when revisiting the same path. This served as a key criterion for quantifying localization accuracy. Second, we examined the overall shape and smoothness of the trajectory. The trajectory shape and smoothness provided insights into the reliability and robustness of localization algorithms.

B. Results and Discussion

Figs. 13 and 14 compare the altitude estimation results for all localization methods in the two testbeds, respectively.

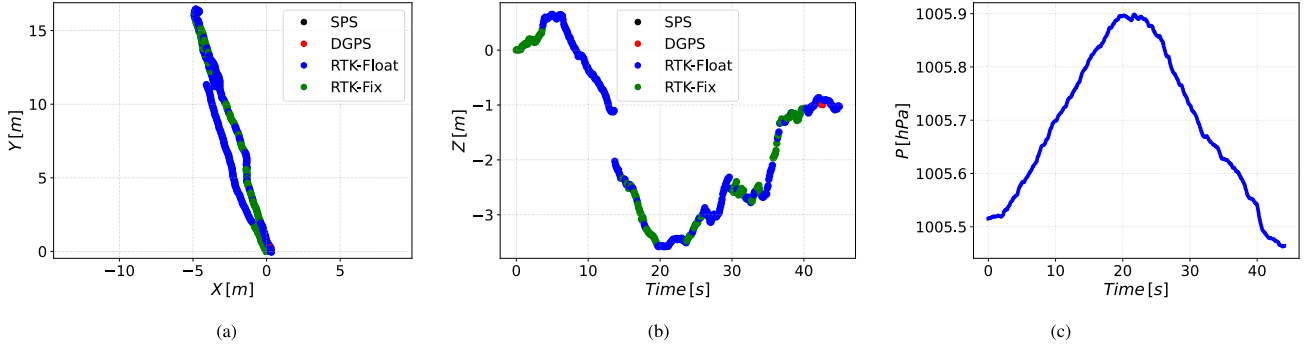
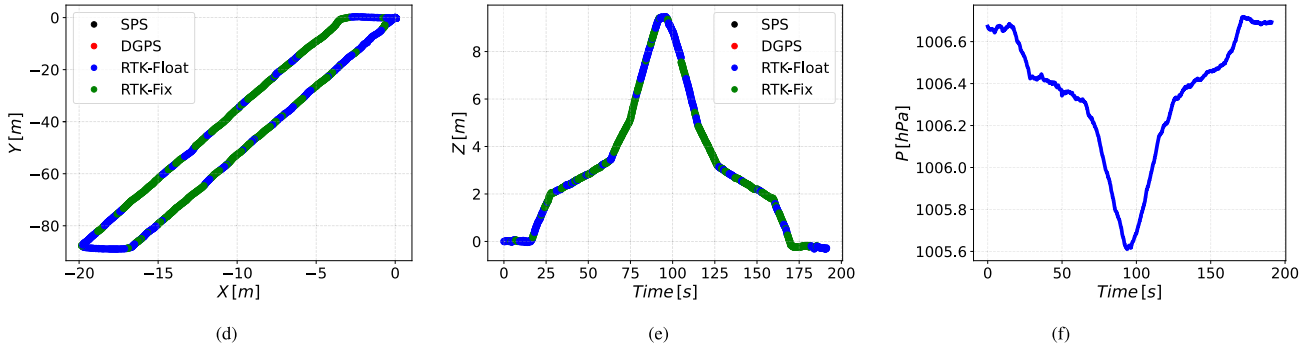
[Testbed 1] Linear reciprocating motion with severe GNSS noise**[Testbed 2]** Rectangular loop motion with various slope changes

Fig. 12. Trajectories and sensor data in two real testbeds. The geodesic GNSS data were transformed from the WGS84 coordinate system to the universal transverse Mercator (UTM) coordinate system. The origin was set as the initial GNSS position. In (d), different aspect ratios were used for the X- and Y-axes to clearly depict the rectangular shape of the trajectory rather than a linear one. (a) and (d) GNSS X-Y. (b) and (e) GNSS Time-Z. (c) and (f) Barometer time-pressure.

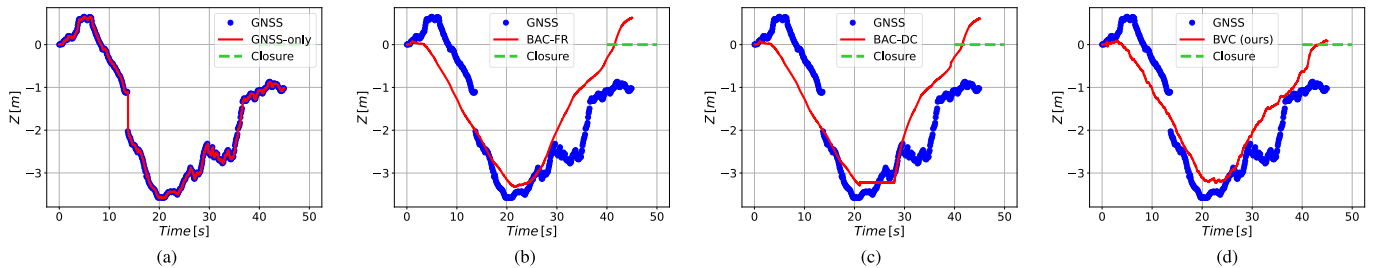


Fig. 13. Altitude estimates of each method in Testbed 1. The expected final altitude is marked as a green dashed line, representing loop closure. (a) GNSS-only [34]. (b) BAC-FR [12]. (c) BAC-DC [15]. (d) BVC (ours).

1) [Testbed 1] Severe GNSS Noise: The integration of barometric data led to significant improvements in altitude estimation across all methods in severe GNSS noise. Notably, all barometric correction methods accurately captured the downward motion during the initial 5-s period and maintained stable estimation through the sudden GNSS anomaly at 13 s. However, as shown in Fig. 13(a), GNSS-only localization failed to overcome erroneous GNSS measurements during the initial 5 s, incorrectly exhibiting an upward trajectory despite the actual downward movement. Furthermore, at nearly 13 s, GNSS-only localization presented its limitations by directly reflecting a sudden jump in the degraded GNSS measurements, ultimately failing to achieve loop closure with approximately 1 m altitude disparity at the end. These results validate the advantages of barometric integration incorporated with GNSS-based localization.

The proposed BVC achieved accurate loop closure at the end, as presented in Fig. 13(d). However, both BAC-FR and BAC-DC methods exhibited noticeable drift in the final trajectory segment due to accumulated barometric bias, as shown in Fig. 13(b) and (c), revealing an inherent limitation of BAC methods.

2) [Testbed 2] Various Slope Changes: Since GNSS noise was not severe, all localization methods produced smooth trajectories for altitude estimates. However, the difference between the methods becomes evident near the loop closure point after 170 s.

The proposed BVC achieved the closest loop closure at the end, as shown in Fig. 14(d). Both BAC-FR and BAC-DC methods suffered from altitude drift after 125 s. Moreover, both BAC methods exhibited altitude undershoots around 175 s. Our test trajectory included one of the most sudden

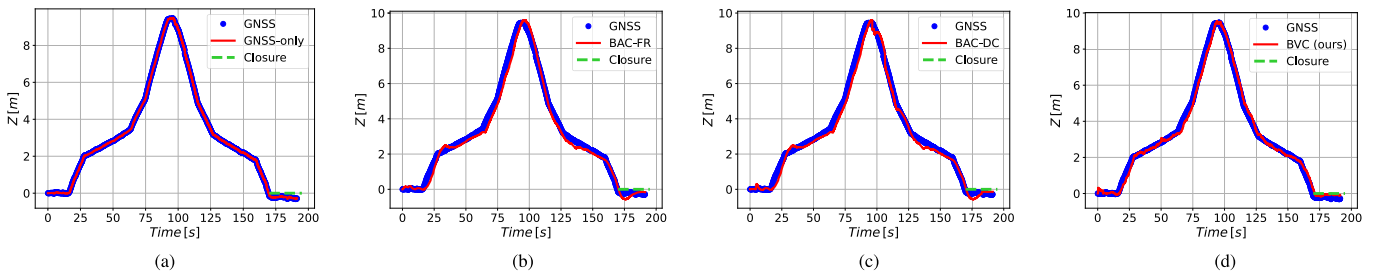


Fig. 14. Altitude estimates of each method in Testbed 2. The expected final altitude is marked as a green dashed line, representing loop closure. (a) GNSS-only [34]. (b) BAC-FR [12]. (c) BAC-DC [15]. (d) BVC (ours).

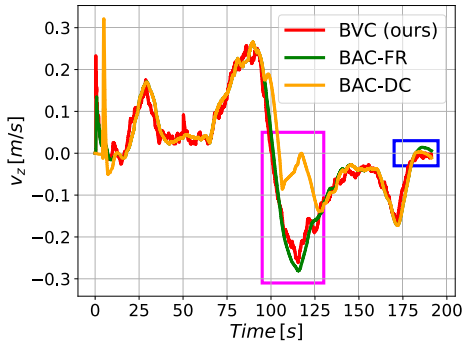


Fig. 15. Vertical velocity estimates of the BAC and BVC in Testbed 2. The blue box indicates the section corresponding to the loop closure in Fig. 14. The expected final velocity is zero. The magenta box presents the section of incorrect velocity estimation in BAC-DC.

altitude changes at 175 s, indicating a significant change in vertical velocity. As shown in the blue box of Fig. 15, EKF localization with BAC-FR and BAC-DC methods did not track the vertical velocity exactly and rapidly, leading to undershoots in their altitude trajectories at that time. Similar phenomena are also observable around other points of slope changes, such as at 30 and 65 s in Fig. 13(b) and (c).

As highlighted in the magenta box in Fig. 15, inaccuracies in velocity estimation are observed in the BAC-DC approach. These inaccuracies are attributed to noise from the inertial-magnetic sensor. A potential mitigation strategy involves increasing the buffer size for drift control; however, this presents another tradeoff, as it cannot guarantee rapid convergence for the drift control. Furthermore, we confirmed that there are limitations in applying this method to cases where geometric motion information from vehicles cannot be utilized, such as drones or hand-held devices.

VI. CONCLUSION

This article proposes a novel BVC that enhances altitude accuracy by integrating GNSS and barometric data. In our experiments with synthetic and real data, two conventional BAC methods exhibit biased altitude estimates due to their direct manner of updating altitude from biased barometric pressures. In contrast, the proposed BVC can overcome this limitation by utilizing barometric data as vertical velocity measurements. In our experiments with synthetic data, the BVC achieved 27.6% lower altitude errors compared to BAC methods and demonstrated more robustness to sensor noises

and parameter uncertainties. Beyond our experimental results, we provided an intuitive idea of how the BVC mitigates accumulated bias errors using (19) and (20). Additionally, in the EKF framework, further theoretical analysis was conducted on concepts of Kalman gain and uncertainty propagation, highlighting adaptive weighting and less uncertainty of the BVC.

We have several directions for further applications and research. First, we plan to apply the proposed barometric integration to outdoor multimodal localization. This will allow us to explore more complex interactions among multimodal sensors such as GNSS, IMU, VIO, and barometers. Second, we aim to extend the proposed barometric velocity approach beyond Bayesian filtering to sliding-window optimization for more accurate and robust localization.

REFERENCES

- [1] B. A. Renfro, M. Stein, E. B. Reed, and E. J. Villalba, “An analysis of global positioning system standard positioning service performance for 2020,” Dept. Space Geophysics Lab. Appl. Res. Laboratories, Univ. Texas at Austin, Austin, TX, USA, Tech. Rep. TR-SGL-21-02, 2021.
- [2] A. Solimeno, “Low-cost INS/GPS data fusion with extended Kalman filter for airborne applications,” Masters thesis, Dept. Aerosp. Eng., Universidade Technica de Lisboa, Lisbon, Portugal, 2007.
- [3] M. G. Petovello, “Real-time integration of a tactical-grade IMU and GPS for high-accuracy positioning and navigation,” Ph.D. thesis, Dept. Geomatics Eng., Univ. Calgary, Calgary, AB, Canada, 2003.
- [4] W. Wen, T. Pfeifer, X. Bai, and L.-T. Hsu, “Factor graph optimization for GNSS/INS integration: A comparison with the extended Kalman filter,” *Navigation*, vol. 68, no. 2, pp. 315–331, Jun. 2021.
- [5] Z. Yue, B. Lian, C. Tang, and K. Tong, “A novel adaptive federated filter for GNSS/INS/VIO integrated navigation system,” *Meas. Sci. Technol.*, vol. 31, no. 8, Aug. 2020, Art. no. 085102.
- [6] Y. Wang, R. Sun, Q. Cheng, and W. Y. Ochieng, “Measurement quality control aided multisensor system for improved vehicle navigation in urban areas,” *IEEE Trans. Ind. Electron.*, vol. 71, no. 6, pp. 6407–6417, Jun. 2024.
- [7] Z. Z. M. Kassas, M. Maaref, J. J. Morales, J. J. Khalife, and K. Shamei, “Robust vehicular localization and map matching in urban environments through IMU, GNSS, and cellular signals,” *IEEE Intell. Transp. Syst. Mag.*, vol. 12, no. 3, pp. 36–52, Fall. 2020.
- [8] X. Liu, W. Wen, F. Huang, H. Gao, Y. Wang, and L.-T. Hsu, “3D LiDAR aided GNSS NLOS mitigation for reliable GNSS-RTK positioning in urban canyons,” 2022, *arXiv:2212.05477*.
- [9] J. S. Ausman, “A Kalman filter mechanization for the baro-inertial vertical channel,” in *Proc. 47th Annu. Meeting Inst. Navigat.*, vol. 47, Jun. 1991, pp. 153–159.
- [10] J. Seo, J. G. Lee, and C. G. Park, “Bias suppression of GPS measurement in inertial navigation system vertical channel,” in *Proc. PLANS. Position Location Navigat. Symp.*, Jun. 2004, pp. 143–147.
- [11] J. Zhang, E. Edwan, J. Zhou, W. Chai, and O. Loffeld, “Performance investigation of barometer aided GPS/MEMS-IMU integration,” in *Proc. IEEE/ION Position, Location Navigat. Symp.*, Apr. 2012, pp. 598–604.

- [12] J. Park, D. Lee, and C. Park, "Implementation of vehicle navigation system using GNSS, INS, odometer and barometer," *J. Positioning, Navigat., Timing*, vol. 4, no. 3, pp. 141–150, Sep. 2015.
- [13] S.-S. Jan, D. Gebre-Egziabher, T. Walter, and P. Enge, "Improving GPS-based landing system performance using an empirical barometric altimeter confidence bound," *IEEE Trans. Aerosp. Electron. Syst.*, vol. 44, no. 1, pp. 127–146, Jan. 2008.
- [14] S. Zhang et al., "A low-cost UAV swarm relative positioning architecture based on BDS/barometer/UWB," *IEEE Sensors J.*, vol. 24, no. 23, pp. 39659–39668, Dec. 2024.
- [15] K.-W. Chiang et al., "Assessment for INS/GNSS/odometer/barometer integration in loosely-coupled and tightly-coupled scheme in a GNSS-degraded environment," *IEEE Sensors J.*, vol. 20, no. 6, pp. 3057–3069, Mar. 2020.
- [16] C.-C. Wang, P.-F. Ho, and J.-C. Chen, "BARLD: Barometer-assisted road-layer detection," *IEEE Trans. Intell. Transp. Syst.*, vol. 23, no. 7, pp. 9226–9239, Jul. 2022.
- [17] J. Wang, W. Chen, J. Shao, D. Weng, and B. Cui, "Robust 3-D velocity-constrained vehicle positioning system: Immunity to variances in smartphone mounting angles," *IEEE Sensors J.*, vol. 25, no. 1, pp. 1313–1322, Jan. 2025.
- [18] J. Wang, D. Weng, X. Qu, W. Ding, and W. Chen, "A novel deep odometry network for vehicle positioning based on smartphone," *IEEE Trans. Instrum. Meas.*, vol. 72, pp. 1–12, 2023.
- [19] K. Muralidharan, A. J. Khan, A. Misra, R. K. Balan, and S. Agarwal, "Barometric phone sensors: More hype than hope?" in *Proc. 15th Workshop Mobile Comput. Syst. Appl.*, Feb. 2014, pp. 1–6.
- [20] G. Liu et al., "Beyond horizontal location context: Measuring elevation using smartphone's barometer," in *Proc. ACM Int. Joint Conf. Pervasive Ubiquitous Comput., Adjunct Publication*, Sep. 2014, pp. 459–468.
- [21] R. Ichikari, L. C. M. Ruiz, M. Kourogi, T. Kurata, T. Kitagawa, and S. Yoshii, "Indoor floor-level detection by collectively decomposing factors of atmospheric pressure," in *Proc. Int. Conf. Indoor Positioning Indoor Navigat. (IPIN)*, Oct. 2015, pp. 1–11.
- [22] Y. Li, W. Chen, J. Wang, and X. Nie, "Precise indoor and outdoor altitude estimation based on smartphone," *IEEE Trans. Instrum. Meas.*, vol. 72, pp. 1–11, 2023.
- [23] H. Qin, Z. Niu, L. Cong, and S. Cao, "Height estimation for pedestrian using nonscenario-based motion mode classification," *IEEE Trans. Instrum. Meas.*, vol. 73, pp. 1–12, 2024.
- [24] B. Ge, H. Zhang, W. Fu, and J. Chen, "Low-cost INS/GNSS integration algorithm aided by multi-constraints applied to vehicle navigation," in *Proc. 5th Int. Conf. Control Robot. Eng. (ICCRE)*, Apr. 2020, pp. 159–163.
- [25] *Standard Atmosphere*, Standard ISO 2533: 1975, Int. Org. for Standardization, 1975.
- [26] J. Parviainen, J. Kantola, and J. Collin, "Differential barometry in personal navigation," in *Proc. IEEE/ION Position, Location Navigat. Symp.*, May 2008, pp. 148–152.
- [27] M. Tanigawa, H. Luinge, L. Schipper, and P. Slycke, "Drift-free dynamic height sensor using MEMS IMU aided by MEMS pressure sensor," in *Proc. 5th Workshop Positioning, Navigat. Commun.*, Mar. 2008, pp. 191–196.
- [28] J. Yun and B. Park, "A GNSS/barometric altimeter tightly coupled integration for three-dimensional semi-indoor mapping with Android smartphones," *IEEE Geosci. Remote Sens. Lett.*, vol. 21, pp. 1–5, 2024.
- [29] E. D. Kaplan and C. Hegarty, *Understanding GPS/GNSS: Principles and Applications*. Norwood, MA, USA: Artech House, 2017.
- [30] L. Ji, R. Sun, Q. Cheng, and J. Wang, "Evaluation of the performance of GNSS-based velocity estimation algorithms," *Satell. Navigat.*, vol. 3, no. 1, p. 18, Sep. 2022.
- [31] C. E. Lin, W. C. Huang, C. W. Hsu, and C. C. Li, "Electronic barometric altimeter in real time correction," in *Proc. IEEE/AIAA 27th Digit. Avionics Syst. Conf.*, Oct. 2008, pp. 1–6.
- [32] K.-I. Na, S. Choi, and J.-H. Kim, "Adaptive target tracking with interacting heterogeneous motion models," *IEEE Trans. Intell. Transp. Syst.*, vol. 23, no. 11, pp. 21301–21313, Nov. 2022.
- [33] S. Choi and J.-H. Kim, "Leveraging localization accuracy with off-centered GPS," *IEEE Trans. Intell. Transp. Syst.*, vol. 21, no. 6, pp. 2277–2286, Jun. 2020.
- [34] S. Yamaguchi and T. Tanaka, "GPS standard positioning using Kalman filter," in *Proc. SICE-ICASE Int. Joint Conf.*, 2006, pp. 1351–1354.
- [35] Kakao Corp. (2024). *Kakao Map*. Accessed: Dec. 26, 2024. [Online]. Available: <https://kko.kakao.com/JFS7DmK2eU>
- [36] Nowon District Office. (2024). *Nowon-gu Waterslide*. Accessed: Dec. 26, 2024. [Online]. Available: https://www.nowon.kr/www/user/bbs/BD_selectBbs.do?q_bbsCode=1027&q_bbsctSn=20240712091516534



Dongwook Heo received the B.S. degree from the Department of Mechanical System Design Engineering, Seoul National University of Science and Technology (SEOULTECH), Seoul, Republic of Korea, in 2022, where he is pursuing the M.S. degree with the Department of Computer Science and Engineering.

His research interests include robot state estimation and 3-D computer vision.



Hyunkil Hwang received the B.S. degree in mechanical and automotive engineering and electrical and information engineering from Seoul National University of Science and Technology (SEOULTECH), Seoul, Republic of Korea, in 2024. He is pursuing the Ph.D. degree with the Department of Mechanical Engineering, University of Delaware, Newark, DE, USA.

His research interests include autonomous navigation, 3-D computer vision, and SLAM.



Jinwon Choi received the B.S. degree from the Department of Mechanical System Design Engineering, Seoul National University of Science and Technology (SEOULTECH), Seoul, Republic of Korea, in 2023 and the M.S. degree from the Department of Computer Science and Engineering, Seoul National University of Science and Technology (SEOULTECH), Seoul, in 2025.

His research interests include 3-D computer vision.



Sunglok Choi received the B.S. degree in mechanical and aerospace engineering from Seoul National University, Seoul, Republic of Korea, in 2006, and the M.S. and Ph.D. degrees in robotics from KAIST, Daejeon, Republic of Korea, in 2008 and 2019, respectively.

From 2008 to 2021, he was a Research Scientist at the Electronics and Telecommunications Research Institute (ETRI), Daejeon. Since 2021, he has been an Assistant Professor with the Department of Computer Science and Engineering, Seoul National University of Science and Technology (SEOULTECH), Seoul. His research interests include autonomous navigation, 3-D computer vision, and robust regression.